ADVANCED MATERIALS
www.advmat.de

Decoupling the Effects of Interface Chemical Degradation and Mechanical Cracking in Solid-State Batteries with Silicon Electrode

Hanyu Huo, Yang Bai, Sebastian Leonard Benz, Timo Weintraut, Shuo Wang, Anja Henss, Dierk Raabe,* and Jürgen Janek**

Silicon is a promising negative electrode material for solid-state batteries (SSBs) due to its high specific capacity and ability to prevent lithium dendrite formation. However, SSBs with silicon electrodes currently suffer from poor cycling stability, despite chemical engineering efforts. This study investigates the cycling failure mechanism of composite Si/Li_6PS_5Cl electrodes by decoupling the effects of interface chemical degradation and mechanical cracking. Chlorine-rich $Li_{5.5}PS_{4.5}Cl_{1.5}$ suppresses interface chemical degradation when paired with silicon, while small-grained Li_6PS_5Cl shows 4.3-fold increase of interface resistance due to large Si/Li_6PS_5Cl contact area for interface degradation. Despite this, small-grained Li_6PS_5Cl improves the microstructure homogeneity of the electrode composites, effectively alleviating the stress accumulation caused by the expansion/shrinkage of silicon particles. This minimizes bulk cracks in Li_6PS_5Cl during the lithiation processes and interface delamination during the delithiation processes. Mechanical cracking shows a dominant role in increasing interface resistance than interface chemical degradation. Therefore, electrodes with small-grained Li_6PS_5Cl show better cycling stability than those with $Li_{5.5}PS_{4.5}Cl_{1.5}$. This work not only provides an approach to decouple the complex effects for cycling failure analysis but also provides a guideline for better use of silicon in negative electrodes of SSBs.

1. Introduction

Current lithium-ion batteries (LIBs) play a pivotal role in modern society due to their widespread use in portable electronic devices, electric vehicles, and renewable energy storage systems.[1] The importance of LIBs lies in their ability to store and deliver energy highly efficient, providing a reliable and scalable power source for a range of applications.[2] While LIBs have been transformative to the mobile electrification of industry, transport, and society, they carry a few fundamental challenges, including safety concerns related to liquid electrolytes (LEs), limited energy density, and decay upon extended charging-discharging cycling. Solid-state batteries (SSBs) present a potential avenue for solving these challenges and leverage a new generation of battery technology.[3] SSBs with solid electrolytes (SEs) eliminate the flammable LEs used in LIBs, potentially enhancing safety and reducing the risk of

H. Huo, S. L. Benz, T. Weintraut, J. Janek
Institute of Physical Chemistry
Justus Liebig University Giessen
Heinrich-Buff-Ring 17, D-35392 Giessen, Germany
E-mail: hanyu.huo@ustc.edu.cn; Juergen.Janek@phys.chemie.uni-giessen.de

H. Huo, S. L. Benz, T. Weintraut, A. Henss, J. Janek
Center for Materials Research (ZfM)
Justus Liebig University Giessen
Heinrich-Buff-Ring 16, D-35392 Giessen, Germany

H. Huo
Department of Materials Science and Engineering
University of Science and Technology of China
Hefei, Anhui 230026, China

Y. Bai
School of Advanced Engineering
Great Bay University
Dongguan 52300, China

S. Wang
Center of Smart Materials and Devices
State Key Laboratory of Advanced Technology for Materials Synthesis and Processing
School of Material Science and Engineering
Wuhan University of Technolog
Wuhan 430070, China

A. Henss
Department of Experimental Physics
Justus Liebig University Giessen
Heinrich-Buff-Ring 16, D-35392 Giessen, Germany

D. Raabe
Max Planck Institute for Sustainable Materials
Max-Planck-Str. 1, 40237 Düsseldorf, Germany
E-mail: d.raabe@mpie.de

The ORCID identification number(s) for the author(s) of this article can be found under https://doi.org/10.1002/adma.202415006

DOI: 10.1002/adma.202415006

thermal runaway reactions. Making them less prone to such self-ignition would eliminate one of the most serious risk factors for safety-critical applications.[4] In addition, SSBs potentially exhibit higher energy density, providing more energy storage capacity in smaller and lighter packages.[5] Increased energy density translates not only to longer-lasting and more powerful batteries, addressing one of the key limitations of this technology, but also to improved overall sustainability of mobile electrified systems due to weight reduction.

However, two critical issues significantly impact the specific capacity, rate performance, and cycling stability of SSBs: interface chemical degradation and mechanical degradation (i.e., cracking). Most oxide, sulfide, and halide SEs exhibit chemical instability upon contact with lithium metal, leading to interface degradation, increased internal cell resistance, and performance deterioration.[6] Furthermore, the resultant uneven distribution of electric current fosters highly localized lithium nucleation and dendrite growth at the interface.[7] This is aggravated during repeated cycling when gradual cyclic stress build-up relaxes in the form of cracks, serving as pathways for lithium dendrite propagation into the SE separators.[8] Apart from interface chemical degradation, SSBs are also prone to mechanical cracking. Even if the volume change upon lithiation/delithiation does not exceed ≈8% for common layered cathode active materials (CAM), the resulting strain at the SE|CAM interfaces stemming from CAM swelling/shrinking, leads to mechanical failure of the SE, thus impeding the ion/electron transport.[9] Understanding the effects of chemo-mechanical degradation is, therefore, an essential prerequisite for the rational design of SSBs with improved interface stability and performance.

Silicon (Si) as a material for the construction of the negative electrode has gained momentum in SSBs due to its high theoretical capacity (3590 mAh g^{-1} based on $Li_{3.75}Si$ at room temperature), abundance, low cost, air stability, and the capability of lithium dendrite suppression.[10] However, SSBs based on Si electrodes exhibit unsatisfactory specific capacity and cycling stability, primarily due to interface chemical degradation and mechanical cracking. These challenges are exacerbated by the continuous volume changes of Si during cycling, which lead to breakdowns and stress-induced damage in the battery. Recently, we revealed the different failure mechanisms of composite Si/Li_6PS_5Cl (LPSCl) and SE-free Si anodes.[11] We found that the continuous growth of the solid electrolyte interphase (SEI) hinders the ion/electron transport at the Si|LPSCl interface, thus entailing poor cycling stability of Si/LPSCl composite electrodes. SE-free Si electrodes enable a 2D planar Si|LPSCl interface, leading to less influence of SEI formation on the cell resistance. However, large stress accumulated at the 2D interface causes void formation and fast capacity decay for the SE-free electrodes. Some studies reported the mechanical cracking at the SE|Si interfaces during the delithiation process of the composite Si anodes, leading to the poor cycling stability. However, quantitative evaluation of interface stress and cracks has not been reported so far.[12] Chemical engineering of microstructures was investigated to improve the electrochemical performance of composite Si electrodes, such as adjusting Si particle size and weight fraction,[13] and selecting SE with different Young's modulus.[14] However, it remains elusive how the changed microstructure affects the effective partial ionic/electronic conductivities, the SEI growth rate and components, and chemo-mechanical coupling. Moreover, these parameters may show opposing influences on the overall electrochemical performance. For example, on the one hand, a small Si particle size decreases the probability of crack formation due to better stress relaxation upon the lithiation/delithiation processes. On the other hand, small Si particles show a high specific surface area, which inevitably causes more SEI formation and irreversible lithium consumption. The stress accumulation at the Si|SE interfaces may cause the SEI layer to separate from the Si particle, thus blocking the interfacial charge transfer. Therefore, decoupling the overlapping effects of chemical degradation and mechanical cracking is important to further optimize the microstructure and improve the performance of SSBs based on Si anodes.

This work aims to decouple the effects of chemical degradation and mechanical cracking to better understand the failure mechanisms of SSBs based on Si anodes. Three different LPSCl SEs, i.e., LPSCl with coarse average particle size (LPSCl@coarse), Cl-rich $Li_{5.5}PS_{4.5}Cl_{1.5}$ (LPSCl@Cl-rich), and LPSCl with small average particle size (LPSCl@small), were mixed with Si particles to obtain Si/LPSCl composites with different microstructure. SEI growth rate and components are quantified by chemical and microstructural characterization, while mechanical cracking is investigated by cross-sectional scanning electron microscope (SEM) images and phase field modeling of the chemo-mechanical coupling. The Si/LPSCl@small composites enable the most homogeneous distribution of Si particles among the three different Si/LPSCl composites, leading to a higher volume fraction of SEI. However, a high tensile stress (1.08 GPa) within the Si/LPSCl@small composite is observed during delithiation, indicating superior interface contact. In contrast, the Si/LPSCl@coarse composite shows low tensile stress (0.98 GPa), which is mitigated by interface crack growth. The increase of the interface resistance is dominated by crack formation rather than SEI formation. Si/LPSCl@small composites show the best cycling stability among the three different Si/LPSCl composites. In addition, Si/LPSCl@small composites show good rate performance due to sufficient ionic/electronic mixed conductivity of Li_xSi alloys during cycling.

2. Quantifying Ionic/Electronic Conductivities of Different Si/LPSCl Composites

LPSCl@coarse, LPSCl@Cl-rich, and LPSCl@small were mixed with Si particles (Si/LPSCl weight ratio of 1:1, corresponding to a Si volume fraction of ≈40% for the pristine unlithiated samples) to fabricate Si/LPSCl composites, respectively. The composites were labeled as Si/LPSCl@coarse, Si/LPSCl@Cl-rich, and Si/LPSCl@small, respectively. The basic information of the three different LPSCl and Si powders we used can be found in the supporting information (Figures S1–S4, Supporting Information). The particle size distributions show that both the LPSCl@coarse and LPSCl@Cl-rich show large particle sizes with D_{50} >10 µm, while D_{50} of LPSCl@small is 3.7 µm. Oxygen is observed as an impurity at the surface of the Si particles, showing SiO_x at the particle surface. The thickness of the SiO_x layer is ≈20 nm.[11] The particle size of the micro-Si used here is in the range of 1–5 µm (D_{50} = 1.6 µm); it has an electronic conductivity of $\sigma_e = 3.1 \times 10^{-5}$ S cm^{-1} at 25 °C in the pristine state (Figure S4, Supporting

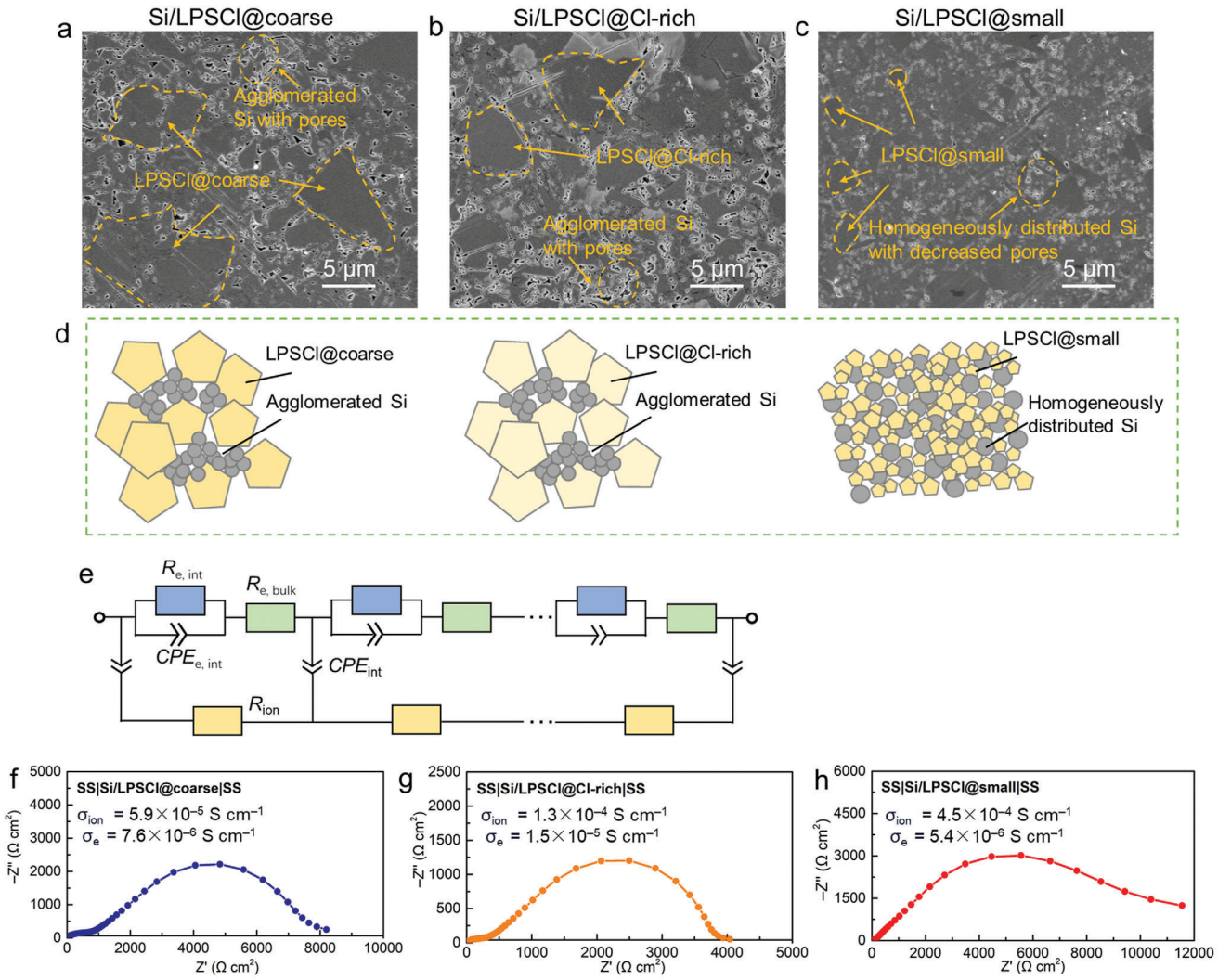

Figure 1. Microstructures and related ion/electron transport in different Si/LPSCl composites. Cross-sectional SEM images of the a) Si/LPSCl@coarse, b) Si/LPSCl@Cl-rich, and c) Si/LPSCl@small composites before cycling. d) Schematic images of microstructures in different Si/LPSCl composites. e) Transmission line model used for fitting the impedance spectra of Si/LPSCl composites. Impedance spectra of the f) SS|Si/LPSCl@coarse|SS, g) SS|Si/LPSCl@Cl-rich|SS, and h) SS|Si/LPSCl@small|SS cell setup.

Information). SEM images show that small Si particles tend to agglomerate at the particle boundaries of the LPSCl@coarse and LPSCl@Cl-rich composites (**Figure** 1a,b, Supporting Information). The agglomerated Si region shows a porous microstructure since the Si particles with a high hardness of ≈10.6 GPa cannot be densified at 380 MPa pressure during fabrication.[15] In contrast, Si particles are homogeneously distributed in the LPSCl@small matrix (Figure 1c,d). The relatively soft LPSCl enables close contact with Si particles after pressing under 380 MPa, leading to an improved density of the Si/LPSCl@small composites.

The impedances of these three Si/LPSCl composites were measured in the symmetric SS|Si/LPSCl|SS cells with stainless steel (SS) electrodes. A transmission line model (TLM) was used to fit the impedances and separate the ionic and electronic contributions in the mixed-conducting Si/LPSCl composites (Figure 1e).[11,16] The two resistor elements $R_{e,bulk}$ (green) and $R_{e,int}$ (blue) in the electronic branch are attributed to electronic bulk transport in the Si and interfacial charge transfer across the Si|Si interfaces, respectively. The resistor element R_{ion} (yellow) in the ionic branch is attributed to ionic bulk transport in the LPSCl SE. We assume that no rate-limiting interfacial charge transfer occurs across the LPSCl|LPSCl interface (i.e., $R_{ion,int} = 0$) due to the densification at 380 MPa. The effective partial ionic and electronic conductivities of the Si/LPSCl@coarse composite are $\sigma_{ion} = 5.9 \times 10^{-5}$ and $\sigma_e = 7.6 \times 10^{-6}$ S cm^{-1} at 25 °C, respectively (Figure 1f). The Si/LPSCl@Cl-rich composite shows both improved ionic and electronic conductivity compared to the Si/LPSCl@coarse composite due to the higher ionic and electronic conductivity of LPSCl@Cl-rich SE (Figure 1g). The Si/LPSCl@small composite exhibits the highest ionic conductivity ($\sigma_{ion} = 4.5 \times 10^{-4}$ S cm^{-1}) among the three Si/LPSCl composites due to the homogeneous microstructure, although the ionic conductivity of LPSCl@small is slightly lower than that of LPSCl@coarse (Figure 1h). However, the small Si particles in

the LPSCl@small are fully embedded in the SE matrix, which lightly blocks the electron transport pathway, causing a comparably low electronic conductivity of the Si/LPSCl@small composite ($\sigma_e = 5.4 \times 10^{-6}$ S cm^{-1}). Clearly, the different effective partial ionic/electronic conductivities affect the specific capacity during the lithiation/delithiation process, which will be discussed later. Overall, both ionic and electronic conductivity are relatively high, being the basis for fast lithiation/delithiation kinetics.

3. SEI Growth Kinetics and Compositions of Different Si/LPSCl Composites

To study the interface degradation in different Si/LPSCl composites, In/InLi|LPSCl|Si/LPSCl cells were rested at the open-circuit voltage (OCV) for ≈16 h after being discharged to $E = -0.6$ V, i.e., to $E = 0.02$ V versus Li$^+$/Li. Figure S5 (Supporting Information) depicts the measurement procedure, wherein impedance spectra were recorded hourly. An In/InLi reference electrode (RE) was centrally positioned within the LPSCl separators and used to separate the positive electrode-related impedance (caused by the Si/LPSCl composite) from the total impedance of the whole cell.[17] The cell setup and lithiation potential of the RE are illustrated in **Figure** 2a. The working electrode (i.e., Si/LPSCl) and counter electrode (i.e., In/InLi foil) in three-electrode cells are the same as those in two-electrode cells. Figure S6 (Supporting Information) exhibits the EIS spectrum (WE vs RE) of the Si/LPSCl composites during testing and the fitted equivalent circuit. The impedance above ≈100 kHz corresponds to ion transport ("IR drop") in the SE separator (R_{SE}) and electrode composite (R_{comp}), while the resistance in the range of 100 kHz–0.5 Hz primarily stems from the contribution at the Si/LPSCl interface (R_{int}).[18] The impedance plots unequivocally demonstrate a gradual increase in R_{int} during the resting period, signifying interfacial degradation. R_{int} increases linearly with the square root of resting time ($t^{0.5}$) as described by a Wagner-type model for diffusion-controlled solid-state reactions (Figure 2b–d).[19] The slope k' corresponds to the SEI growth rate at the Si|LPSCl interface. For Si/LPSCl@coarse it results as $k' = 9.8\ \Omega\ h^{-0.5}$. For Si/LPSCl@Cl-rich it is $k' = 2.9\ \Omega\ h^{-0.5}$, indicating less SEI formation. Consequently, Cl-rich LPSCl shows enhanced electrochemical stability at low potentials, mitigating severe interfacial degradation. In contrast, LPSCl@small facilitates a more homogeneous Si distribution. The increased interface area between the Si particles and the LPSCl results in more SEI formation for Si/LPSCl@small, thus leading to a high value of $k' = 12.4\ \Omega\ h^{-0.5}$. It is noteworthy that k' describes the formation of the SEI in an interconnected 3D composite, rendering it an operational descriptor that is not readily interpreted in terms of a solid-state reaction in 1D geometry and a well-defined thickness of the reaction layer. However, it well describes the formation of resistive SEI regions in the 3D composite quantitatively.

Time-of-flight secondary ion mass spectrometry (ToF-SIMS) was used to verify the local decomposition of the LPSCl electrolyte in the composite Si/LPSCl anodes after 100 cycles. ToF-SIMS is capable of detecting even minute compositional changes on the surface, rendering it a valuable method for identifying decomposition products at interfaces.[20] The analysis of the composite surface after 100 cycles, shown in Figure 2e, illustrates an increase in LiS^- signal intensities for all Si/LPSCl composites. This increase is attributed to interfacial decomposition products of LPSCl (i.e., Li_3P, Li_2S, and LiCl), as recently demonstrated by Walther et al.[21] However, the increase of the intensity of the LiS^- signal follows the sequence Si/LPSCl@Cl-rich < Si/LPSCl@coarse < Si/LPSCl@small, indicating reduced SEI formation in the Si/LPSCl@Cl-rich and enhanced SEI formation in the Si/LPSCl@small composite compared to the Si/LPSCl@coarse composite. These results align well with the SEI growth rate described by k' and are also confirmed by X-ray photoelectron spectroscopy (XPS) measurements. The strong double peaks at 161.7 eV and very small double peaks at 160.1 eV in the S 2p spectrum before cycling originate from the PS_4^{3-} tetrahedra and "free" S^{2-} ions of the argyrodite LPSCl structure, respectively (Figure 2f).[21] The increased intensity of the double peaks at 160.1 eV in the S 2p spectrum after 100 cycles, which corresponds to Li_2S, comes from the LPSCl decomposition with lithium. In addition, double peaks at 166.8 eV corresponding to SO_3^{2-} are observed for the Si/LPSCl@small material after 100 cycles, indicating the reaction of LPSCl and its SEI components with SiO_x impurity on the surface of the Si particles and more severe interface degradation.

To delve deeper into the SEI structure and components at the Si/LPSCl interface, XPS depth profiling was conducted on the Si/LPSCl@small composite after 100 cycles. (Figure 2g–i). The SEI at the Si/LPSCl interface shows a layered structure, where the intensity of LPSCl-induced SEI (e.g., Li_2S) decreases during the sputtering with Ar^+ ions (Figure 2g). Notably, the SiO_x impurity at the Si particle surface contributes to the SEI formation on the bottom of the LPSCl-induced SEI.[22] SiO_2 (≈102.9 eV) and Li_xSiO_y (≈101.4 eV) are observed in the Si 2p spectra due to the reaction between SiO_x and lithium.[23] We assume that the disproportionation of SiO_x, represented by the reaction $SiO_x = x/2\ SiO_2 + (1\text{-}x/2)$ Si, may then lead to the formation of a Li_xSiO_y phase (Figure 2h). The presence of irreversible lithium is evidenced by the emergence of a Li-Si peak at ≈98.0 eV in the Si 2p spectrum, exhibiting increased intensity during Ar^+ ion sputtering. In addition, Li_xO (≈531.4 eV) and Li_2O (≈528.6 eV) are observed in the O 1s spectra, further confirming the reaction between SiO_x and lithium (Figure 2i). A schematic image in Figure 2j shows the SEI structure at the Si/LPSCl interfaces.

Cells with In/InLi counter electrodes were cycled at 0.1 C to compare the specific capacity of different Si/LPSCl composites. As depicted in Figure S7 (Supporting Information), the Si/LPSCl@Cl-rich composite delivers the highest specific capacity of q_m ≈2800 mAh g^{-1} with the smallest SEI capacity contribution (q_m ≈170 mAh g^{-1}) among the three different Si/LPSCl composites. This can be attributed to the lowest k' value for the SEI growth and the improved ionic/electronic conductivity of the Si/LPSCl@Cl-rich composite. The initial Coulomb efficiency of the Si/LPSCl@coarse, Si/LPSCl@Cl-rich, and Si/LPSCl@small is 88.9%, 90/3%, and 79.7%, respectively. The Si/LPSCl@Cl-rich shows the highest Coulomb efficiency, which is consistent with the results of k' for the SEI growth. Moreover, from the viewpoint of SEI growth, the Si/LPSCl@small composite should show the worst cycling performance among these three Si/LPSCl composites due to the highest k' value for continuous SEI growth. Surprisingly, the Si/LPSCl@small composite shows the highest capacity retention (i.e., 45.1%) after 100 cycles at 0.1 C,

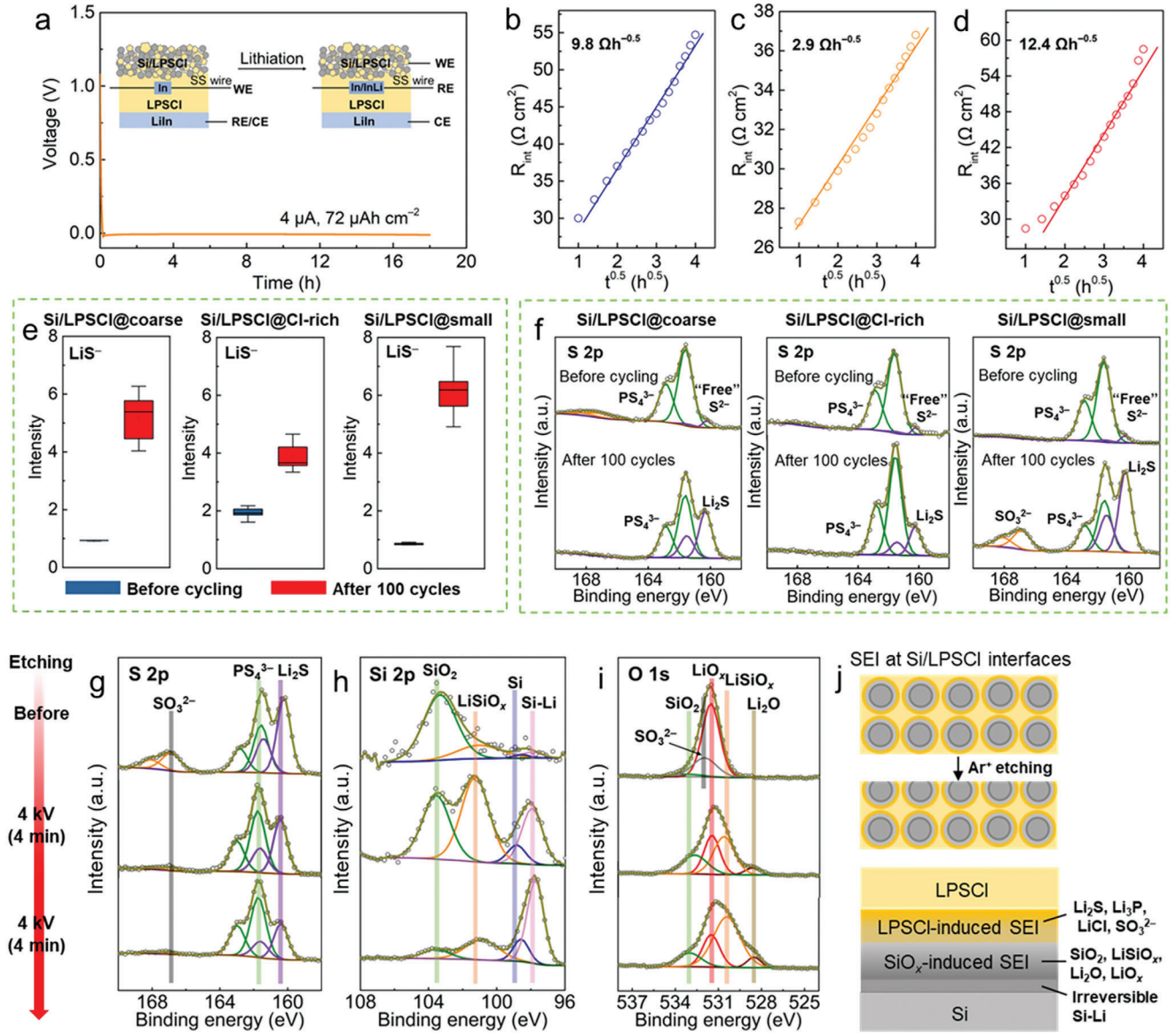

Figure 2. Interface chemical degradation of different Si/LPSCl composites. a) Lithiation of the In wire as reference electrode for the three-electrode cell. R_{int} as a function of the square root of time ($t^{0.5}$) in (b) the Si/LPSCl@coarse, c) Si/LPSCl@Cl-rich, and d) Si/LPSCl@small composites. (e) Box plots of SEI-related signal intensities (i.e., LiS^-) from ToF-SIMS surface analyses of different Si/LPSCl composites before and after 100 cycles. f) S 2p XPS spectra of different Si/LPSCl composites before and after 100 cycles. g) S 2p, h) Si 2p, and i) O 1s XPS depth profiles of the Si/LPSCl@small anodes after 100 cycles. 2 kV for 4 min was first operated before 4 kV operation. j) Sketch of the SEI microstructure at the Si/LPSCl interfaces.

compared to the Si/LPSCl@coarse (i.e., 26.6%) and Si/LPSCl@Cl-rich composites (31.7%) (**Figure** 3a). The capacity retention of the Si/LPSCl@small composite is also the highest at 0.5 C (Figure S8, Supporting Information). Even if the Si/LPSCl@Cl-rich composite leads to less SEI growth, the cycling stability is better than that of the Si/LPSCl@coarse composite, but still inferior to that of the Si/LPSCl@small composite (Figure 3a). We measured EIS based on a three-electrode cell setup to evaluate R_{int} of the three different Si/LPSCl electrodes during cycling (Figure S9 and Tables S5–S7, Supporting Information). The Si/LPSCl@small electrode shows the lowest increase of R_{int} after 20 cycles compared with the other two composite electrodes, which explains the best cycling performance, although similar R_{int} values were observed after the 1st cycle (Figure 3b). These results underscore that the SEI growth is not the sole determinant of the increase in the interface resistance, which significantly impacts the ion/electron transport at the interfaces and thereby profoundly influences cycling stability.

4. Cycling Stability and Microstructure Evolution of Different Si/LPSCl Composites

The evolution of microstructure in different Si/LPSCl composite electrodes is compared to gain deeper insights into the

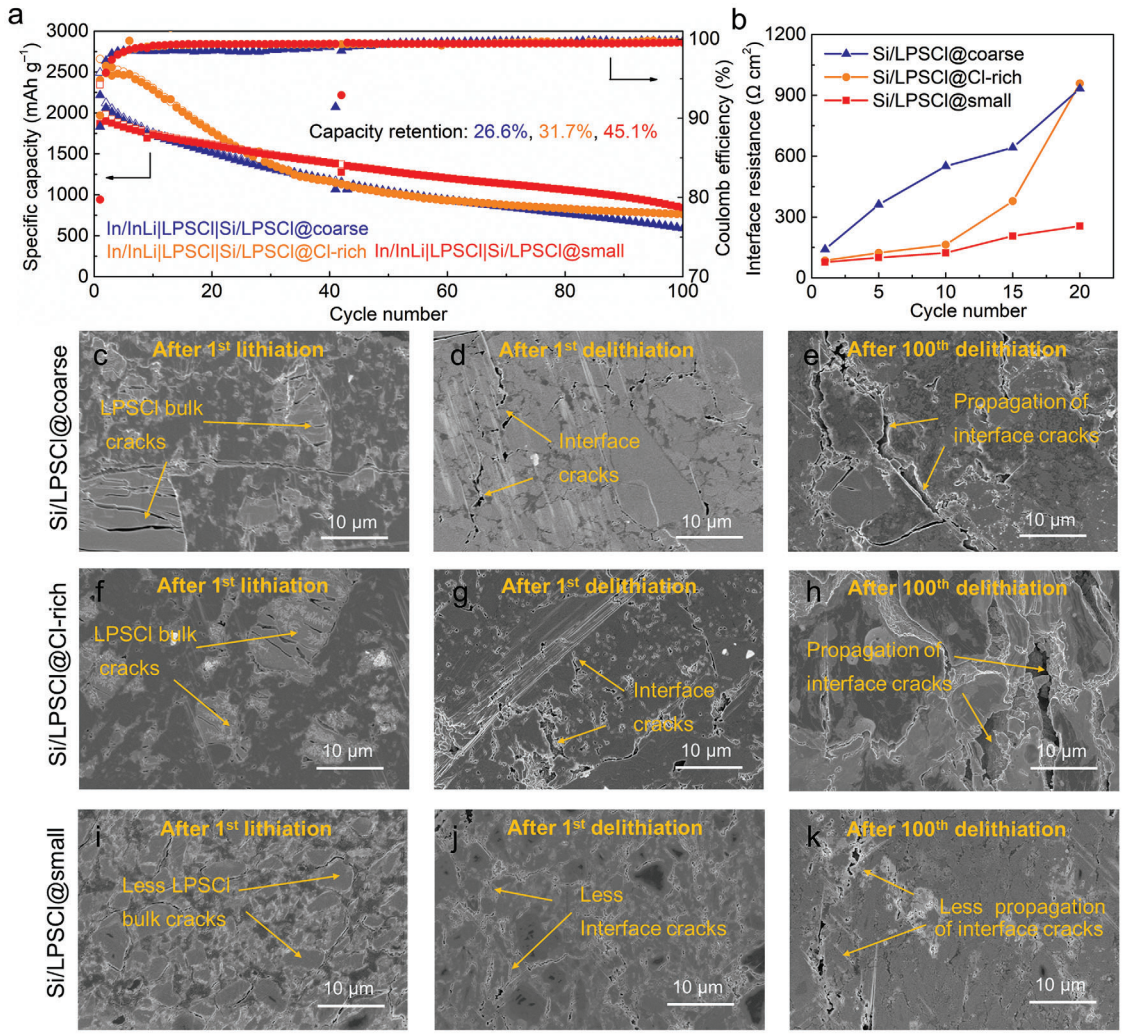

Figure 3. Cycling stability and microstructure evolution of different Si/LPSCl composites. a) Comparison of cycling performance between different Si/LPSCl composites at 0.1 C under 50 MPa. b) Interface resistance of different Si/LPSCl composites during cycling. Cross-sectional SEM images of the Si/LPSCl@coarse electrode c) after the 1st lithiation, d) after the 1st delithiation, and e) after the 100th delithiation. Cross-sectional SEM images of the Si/LPSCl@Cl-rich electrode, f) after the 1st lithiation, g) after the 1st delithiation, and h) after the 100th delithiation. Cross-sectional SEM images of the Si/LPSCl@small electrode i) after the 1st lithiation, j) after the 1st delithiation, and k) after the 100th delithiation.

effects of chemo-mechanics on cycling stability. The LPSCl and Li_xSi regions can be distinguished by the cross-sectional SEM images and corresponding energy dispersive spectroscopy (EDS) mappings (Figure S10, Supporting Information). The lithiation of Si particles exhibits an elastic softening effect, gradually reducing the Young´s modulus of the resulting Li_xSi alloy from 168 GPa (pristine Si) to 41 GPa ($Li_{3.75}Si$).[24] Si expansion under a 50 MPa constraining pressure therefore tends to densify the microstructure of the relatively soft Li_xSi regions, leading to an interconnected Li_xSi microstructure upon the 1st lithiation (Figure 3c,f). Although the Si|LPSCl interfaces remain intact, crack formation inside the LPSCl particles is observed for both Si/LPSCl@coarse and Si/LPSCl@Cl-rich composites due to the internal stress generated by Si expansion (Figure 3c,f). Additionally, submicron-sized cracks are observed at the Si|LPSCl interfaces after the 1st delithiation due to the shrinkage of Si (Figure 3d,g). These submicron-scaled cracks further develop, propagate, and widen after the 100th delithiation (Figure 3e,h). In contrast, the Si/LSPCl@small composite shows fewer LPSCl bulk cracks upon the 1st lithiation and less interface crack formation and propagation after the 1st and 100th delithiation, compared to the Si/LPSCl@coarse and Si/LPSCl@Cl-rich composites. The homogeneously distributed Si particles in the LPSCl@small matrix effectively alleviate stress from the volume change of Si during cycling. We note that the Si/LPSCl|LPSCl separator interface maintains close contact after 100 cycles for all three different Si/LPSCl anodes (Figure S11, Supporting Information).

5. Chemo-Mechanical Phase-Field Models

A fully coupled chemo-mechanical phase-field model including damage was applied to evaluate the elastoplastic deformation and the stress-induced fractures of different Si/LPSCl anodes

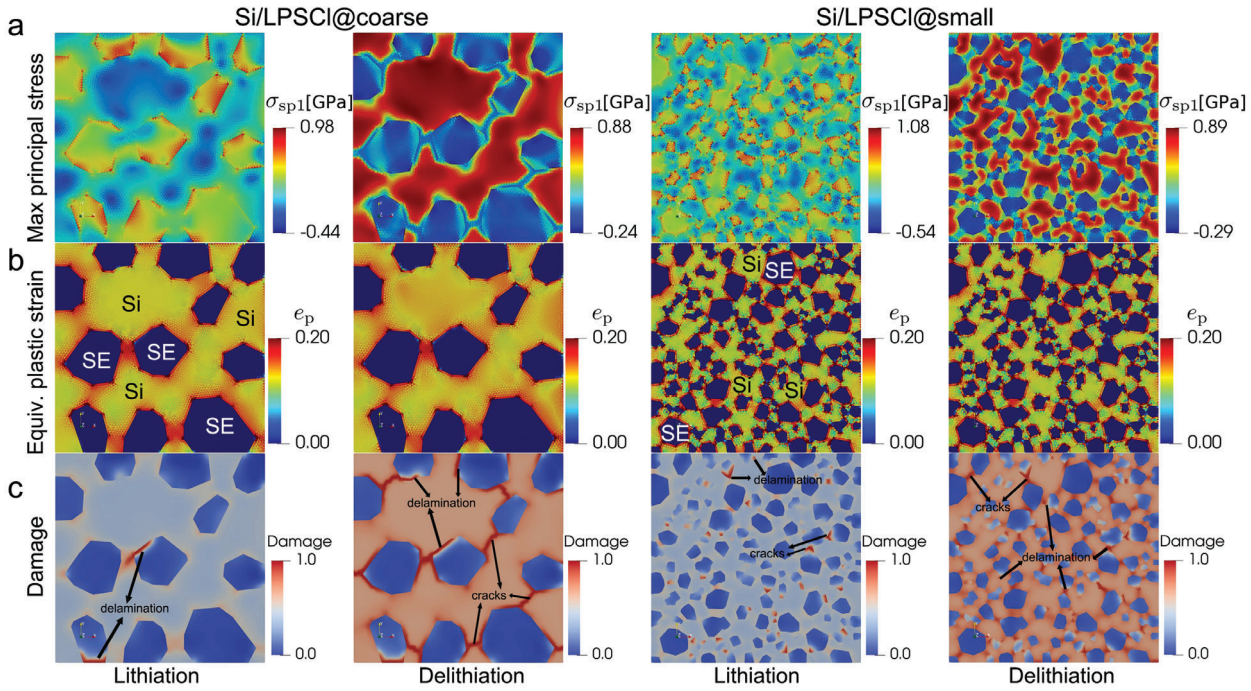

Figure 4. Chemo-mechanical phase-field models showing SE particle effects. Results on micromechanics and internal damage in composite Si/LPSCl anodes obtained from a fully coupled chemo-mechanical phase-field model that includes damage. The simulations used the same volume fractions but different dispersion of the two phases in the anode composite. Comparison of a) maximum principal stress, b) equivalent (von Mises) plastic strain, and c) resulting crack patterns between the Si/LPSCl@coarse and Si/LPSCl@small composites at the end of the lithiation and delithiation processes.

(Figure S12, Supporting Information). While the elastic contribution considers the linear change in lattice parameter upon Li alloying and de-alloying and translates it into a Hooke stress, the plastic part refers to the inelastic deformation of the composite (mediated through dislocations) which occurs when the stress exceeds the elastic limit (flow stress). Damage is initiated and develops if the total local mechanical energy density cannot be compensated by elastic and plastic deformation alone. Details of the underlying phase field formulations are given in the Supporting Information. The simulations reveal that upon completion of the lithiation process, both Si/LPSCl@coarse and Si/LPSCl@small composites exhibit a uniform lithium distribution (low lithium concentration gradient) (Figure S13, Supporting Information). The dimensionless concentration c_{Li} within the Si particles (defined in the SI as the amount of lithium relative to the maximum available sites c_{max} in Si) reaches nearly 1.0 (i.e., $Li_{4.2}Si$). Upon completion of the lithiation process, the substantial expansion of the Si particles of about 20% (the theoretical expansion could potentially reach 300%, however, to maintain numerical stability and avoid the mesh distortion in the phase field model, a value of 20% is employed for the complex composite electrode in this study) induces a pronounced maximum principal stress σ_{sp1} at the Si|LPSCl interfaces within both, the Si/LPSCl@coarse (approximately 0.98 GPa) and Si/LPSCl@small (≈1.08 GPa) composites, as illustrated in **Figure** 4a. Simultaneously, a notable quantity of equivalent plastic strain (≈20% in both Si/LPSCl@coarse and Si/LPSCl@small composites) accumulates at this interface owing to the elevated stress levels that originate from the swelling of the Si particles upon Li alloying, as depicted in Figure 4b. Yet, the overall large internal stress build-up cannot be compensated by the additional plastic deformation alone so that cracks evolve and grow, a mechanism which leads to a significant relaxation of the local stress levels owing to material coherency loss (i.e., damaged regions cannot carry or mediate stresses). Consequently, the observation of higher tensile stress (1.08 GPa) within the Si/LPSCl@small anode implies superior interface contact compared to the Si/LPSCl@coarse anode, where the lower simulated stress (0.98 GPa) is caused by crack growth and the associated material coherency loss. Figure 4c shows numerous instances of interface delamination (cracks) in the Si/LPSCl@coarse composite, whereas only minimal delamination is observed in the Si/LPSCl@small composite.

By the end of the delithiation process, the lithium concentration within the Si particles drops nearly to zero ($c_{Li}/c_{max} \approx 0.02$ in the Si/LPSCl@coarse composite, and $c_{Li}/c_{max} \approx 0.03$ in the Si/LPSCl@small composite) (Figure S13, Supporting Information). "Delamination" refers to cracks at the Si|LPSCl interface that can completely disconnect between Si particles and the SE. In contrast, "cracks" describe mechanical failures within the Si particles and the SE itself. As previously noted, a substantial amount of the simulated equivalent plastic strain is generated at the end of the lithiation process in both electrodes. Consequently, the shrinkage effect exhibited by Si particles during delithiation induces additional elastoplastic deformation within the material. This subsequent deformation has the potential to initiate further cracking within the composite Si anodes. As depicted in Figure 4c, the Si/LPSCl@coarse composite indeed experiences significant interface delamination as well as trans-particle cracks

within the Si. These cracks serve to further alleviate stresses. Hence, it is observed that the maximum principal stress σ_{sp1} in the Si/LPSCl@coarse composite (≈0.88 GPa) is marginally lower than during lithiation. The same conclusion applies to the Si/LPSCl@small composite, where its maximum principal stress σ_{sp1} is decreased from 1.08 to 0.89 GPa at the end of delithiation. Concurrently, the Si/LPSCl@small electrode also shows a greater volume fraction of cracks (interface delamination and transparticle cracks occupy ≈50% of the simulated area) compared to the lithiation process (crack volume fraction is ≈30%). Furthermore, the interface region depicted in Figure 4b exhibits higher equivalent plastic strain due to the increased elastoplastic deformation.

These findings suggest that the interface within the Si/LPSCl@coarse composite exhibits greater susceptibility to damaging stress accumulation compared to the Si/LPSCl@small anode, thereby facilitating accelerated crack growth and thus poorer interface contact. Throughout lithiation/delithiation, these cracked regions propagate and percolate significantly, mitigating further stress build-up at the interfaces, due to coherency loss. Consequently, at the end of the process, the Si/LPSCl@small composite continues to endure higher stress levels compared to the Si/LPSCl@coarse composite. Thus, the homogeneous microstructure of the Si/LPSCl@small composite with a smaller particle size of the LPSCl contributes to improved interface contact and enhanced mechanical strength, as evidenced by less occurrence of interface delamination and cracking. A finer dispersion in such composite composites thus causes altogether a more moderate and homogeneous internal stress evolution, less stress peaks at interfaces, and therefore also less cracking.

We further delve into the interface damage fraction to quantify the percentage of delamination or the interface's structural degradation per unit length dL along the interface Γ between the Si and the LPSCl SE. The order parameter d denotes the damage field, with $d = 1$ indicating a fully broken case, while $d = 0$ signifies an undamaged case. The percentage of the interface delamination can be computed by integrating $\int_{\Gamma} d \, \mathrm{d}L$., where a value of 100% signifies a fully fractured or delaminated interface between the Si and LPSCl SE. As illustrated in Figure S14a (Supporting Information), the interface delamination fraction of the Si/LPSCl@coarse composite (≈45%) is marginally lower than that of the Si/LPSCl@small composite (≈52%) at the end of the lithiation process. Moreover, this difference becomes more pronounced during the delithiation process. The delamination fraction of the Si/LPSCl@small composite is 10% lower than that of the Si/LPSCl@coarse composite. Furthermore, the volume-averaged maximum principal stress σ_{sp1} (i.e., the average maximum principal stress per unit volume) of the Si/LPSCl@small composite is ≈300 MPa at the end of delithiation, which is 100 MPa less than that of the Si/LPSCl@coarse composite (Figure S14b, Supporting Information) These results confirm that the improved microstructure homogeneity of composite Si/LPSCl electrodes by decreasing the LPSCl particle size is beneficial to alleviate stresses and decrease cracks, thereby enhancing interface contact and cycling performance. In addition, increasing the external pressure can further suppress the formation of interface cracks (Figure S15, Supporting Information).

6. Full Cell Evaluation Based on Si/LPSCl@small|LPSCl|NCM@LBO Cells

To evaluate the electrochemical performance in full cells, composite $LiNi_{0.83}Co_{0.11}Mn_{0.06}O_2$ (NCM) (positive) electrodes were paired with Si/LPSCl@small electrodes with an N/P ratio of 1.3. The surface of the NCM particles was coated with a thin layer (2 nm) of $Li_2B_4O_7$ (LBO) to prevent electrochemical degradation at the NCM|LPSCl interface. Composite NCM electrodes (NCM@LBO) were fabricated by mixing with NCM@LBO, LPSCl@small, and vapor-grown carbon fiber (VGCF) with the ratio of NCM@LBO: LPSCl@small: VGCF = 80:20:3. A cross-section SEM image shows a homogeneous distribution of NCM particles in the LPSCl matrix, which enables sufficient ion/electron transport (Figure S16, Supporting Information). The Si/LPSCl@small|LPSCl|NCM@LBO cells deliver a specific discharge capacity (based on NCM mass) of 156.9, 137.6, 91.5, and 66.3 mAh g^{-1} at 0.1 C, 0.2 C, 0.5 C, and 1 C, respectively (Figure S17a, Supporting Information). The good rate performance comes from the high ionic/electronic conductivity of Li_xSi within the Si/LPSCl@small electrodes during cycling.[11] The Si/LPSCl@small|LPSCl|NCM@LBO cells can successfully operate 100 cycles with a capacity retention of 51.9% at 0.1 C (Figure S17b, Supporting Information). Full SSB cells normally exhibit worse cycling performance compared to half cells due to the fast lithium loss by irreversible capacities in both negative and positive electrodes. However, Si/LPSCl@small|LPSCl|NCM@LBO full cells show better capacity retention than In/InLi|LPSCl|Si/LPSCl@small half cells (51.9% vs 45.1%). Our recent work revealed that a positive pressure change (i.e., $p > 50$ MPa) of full cells helps to maintain cycling stability compared to a negative pressure change of half cells (i.e., $p < 50$ MPa) during cycling.[11] Operando imaging techniques (e.g., X-ray tomography) may be powerful to monitor the morphology evolution and pressure change in the Si-based SSBs in real time which will be part of future work.[25]

In summary, we explored the failure mechanisms of composite Si/LPSCl anodes by decoupling the effects of interface chemical degradation, i.e., SEI formation, and mechanical cracking. LPSCl@coarse, LPSCl@Cl-rich, and LPSCl@small were mixed with Si particles to fabricate different composite Si/LPSCl electrodes, respectively. SEI growth kinetics is quantified by impedance analysis of the three-electrode cell setup, where the rate constant k' describes the resistance increase of the 3D composite due to SEI growth. Si/LPSCl@small composites exhibit a larger k' (12.4 Ω $h^{-0.5}$) compared to the Si/LPSCl@coarse (9.8 Ω $h^{-0.5}$) and Si/LPSCl@Cl-rich (2.9 Ω $h^{-0.5}$) composites attributed to a larger Si/LPSCl contact area, indicating a more pronounced effect of chemical interface degradation. XPS and SIMS results reveal that SEI components encompass not only the decomposition products of LPSCl, but also involve the SiO_x impurity on the surface of Si particles in the SEI formation. Mechanical cracking plays a primary role in increasing interface resistance compared to SEI formation. Despite exhibiting the highest k' for SEI growth, Si/LPSCl@small composite electrodes show the best cycling stability among the three composite Si/LPSCl electrodes. This is attributed to increased homogeneity in the microstructure of Si/LPSCl@small composites, which reduced both bulk crack formation of LPSCl particles

during lithiation and interface delamination during delithiation. Phase-field fracture modeling further reveals high tensile stress (1.08 GPa) within the Si/LPSCl@small composites, indicating superior interface contact. In contrast, low stress (0.98 GPa) is obtained for the Si/LPSCl@coarse anode due to the mitigation by crack growth. This work presents a benchmark approach for battery failure analysis and provides a first guideline for the microstructure optimization of composite Si anodes. Once microstructure optimization is combined with mitigation of SEI formation through the chemical design of the SE (e.g., small-sized Cl-rich LPSCl), cell function can further improve.

Supporting Information

Supporting Information is available from the Wiley Online Library or from the author.

Acknowledgements

The authors acknowledge financial support from the Federal Ministry of Education and Research (BMBF, Bundesministerium für Bildung und Forschung) within the FESTBATT consortium (03XP0430A, 03XP0433D) and the project SILKOMPAS (03XP0486D), the DFG for funding of the Hybrid-SIMS (M6 Hybrid SIMS, IONTOF GmbH, Muenster, Germany) under grant number INST 162/544-1 FUGG. S.W. acknowledges the Natural Science Foundation of China (grant no. 52302305).

Open access funding enabled and organized by Projekt DEAL.

Conflict of Interest

The authors declare no conflict of interest.

Author contributions

H.H. and Y.B. contributed equally to this work. H.H. conceived and designed the experimental work and prepared the manuscript; Y.B. and D.R. carried out the chemo-mechanical modeling; S.L.B. operated the XPS measurements; T.W. and A.H. operated the SIMS measurements; S.W. synthesized the Cl-rich LPSCl electrolyte; J.J. supervised the overall project and revised the manuscript. All authors have given approval to the final version of the manuscript.

Data Availability Statement

Research data are not shared.

Keywords

chemo-mechanics, silicon anodes, solid electrolytes, solid-state batteries

Received: October 2, 2024
Revised: November 11, 2024
Published online: December 20, 2024

[1] a) T. Krauskopf, F. H. Richter, W. G. Zeier, J. Janek, *Chem. Rev.* **2020**, *120*, 7745; b) C. Wang, K. Fu, S. P. Kammampata, D. W. McOwen, A. J. Samson, L. Zhang, G. T. Hitz, A. M. Nolan, E. D. Wachsman, Y. Mo, V. Thangadurai, L. Hu, *Chem. Rev.* **2020**, *120*, 4257; c) X. B. Cheng, R. Zhang, C. Z. Zhao, Q. Zhang, *Chem. Rev.* **2017**, *117*, 10403.

[2] a) J.-M. Tarascon, M. Armand, *Nature* **2001**, *414*, 359; b) M. Armand, J.-M. Tarascon, *Nature* **2008**, *451*, 652.

[3] a) J. Janek, W. G. Zeier, *Nat. Energy* **2016**, *1*, 1; b) J. Janek, W. G. Zeier, *Nat. Energy* **2023**, *8*, 230.

[4] R. Chen, W. Qu, X. Guo, L. Li, F. Wu, *Mater. Horiz* **2016**, *3*, 487.

[5] S. Randau, D. A. Weber, O. Kötz, R. Koerver, P. Braun, A. Weber, E. Ivers-Tiffée, T. Adermann, J. Kulisch, W. G. Zeier, *Nat. Energy* **2020**, *5*, 259.

[6] a) K. H. Park, Q. Bai, D. H. Kim, D. Y. Oh, Y. Zhu, Y. Mo, Y. S. Jung, *Adv. Energy Mater.* **2018**, *8*, 1800035; b) L. Zhou, N. Minafra, W. G. Zeier, L. F. Nazar, *Acc. Chem. Res.* **2021**, 19002; c) X. Li, J. Liang, X. Yang, K. R. Adair, C. Wang, F. Zhao, X. Sun, *Energy & Environ. Sci.* **2020**, *13*, 1429.

[7] J. Kasemchainan, S. Zekoll, D. Spencer Jolly, Z. Ning, G. O. Hartley, J. Marrow, P. G. Bruce, *Nat. Mater.* **2019**, *18*, 1105.

[8] Z. Ning, D. S. Jolly, G. Li, R. De Meyere, S. D. Pu, Y. Chen, J. Kasemchainan, J. Ihli, C. Gong, B. Liu, *Nature Mater* **2021**, *20*, 1121.

[9] a) R. Koerver, I. Aygün, T. Leichtweiß, C. Dietrich, W. Zhang, J. O. Binder, P. Hartmann, W. G. Zeier, J. Janek, *Chem. Mater.* **2017**, *29*, 5574; b) T. Shi, Y.-Q. Zhang, Q. Tu, Y. Wang, M. Scott, G. Ceder, *J. Mate. Chem. A* **2020**, *8*, 17399.

[10] a) H. Huo, J. Janek, *ACS Energy Lett.* **2022**, *7*, 4005; b) X. Zhan, M. Li, S. Li, X. Pang, F. Mao, H. Wang, Z. Sun, X. Han, B. Jiang, Y.-B. He, *Energy Storage Mater.* **2023**, 102875.

[11] H. Huo, M. Jiang, Y. Bai, S. Ahmed, K. Volz, H. Hartmann, A. Henss, C. V. Singh, D. Raabe, J. Janek, *Nat. Mater.* **2024**, *23*, 543.

[12] a) J. Tao, J. Han, Y. Wu, Y. Yang, Y. Chen, J. Li, Z. Huang, Y. Lin, *Energy Storage Mater.* **2024**, *64*, 103082; b) D. Cao, T. Ji, A. Singh, S. Bak, Y. Du, X. Xiao, H. Xu, J. Zhu, H. Zhu, *Adv. Energy Mater.* **2023**, *13*, 2203969.

[13] a) J. E. Trevey, K. W. Rason, C. R. Stoldt, S.-H. Lee, *Electrochem. Solid-State Lett.* **2010**, *13*, A154; b) N. A. Dunlap, S. Kim, J. J. Jeong, K. H. Oh, S.-H. Lee, *Solid State Ion* **2018**, *324*, 207.

[14] A. Kato, M. Yamamoto, A. Sakuda, A. Hayashi, M. Tatsumisago, *ACS Appl. Energy Mater.* **2018**, *1*, 1002.

[15] V. Kulikovsky, V. Vorlíček, P. Boháč, M. Stranyánek, R. Čtvrtlík, A. Kurdyumov, *Thin Solid Films* **2008**, *516*, 5368.

[16] P. Minnmann, L. Quillman, S. Burkhardt, F. H. Richter, J. Janek, *J. Electrochem. Soc.* **2021**, *168*, 040537.

[17] T.-T. Zuo, R. Rueß, R. Pan, F. Walther, M. Rohnke, S. Hori, R. Kanno, D. Schröder, J. Janek, *Nat. Commun.* **2021**, *12*, 6669.

[18] W. Zhang, D. A. Weber, H. Weigand, T. Arlt, I. Manke, D. Schröder, R. Koerver, T. Leichtweiss, P. Hartmann, W. G. Zeier, *ACS Appl. Mater. Interfaces* **2017**, *9*, 17835.

[19] a) T. Hoar, L. Price, *Trans. Faraday Society* **1938**, *34*, 867b; b) S. Wenzel, S. Randau, T. Leichtweiß, D. A. Weber, J. Sann, W. G. Zeier, J. r. Janek, *Chem. Mater.* **2016**, *28*, 2400.

[20] T. Lombardo, F. Walther, C. Kern, Y. Moryson, T. Weintraut, A. Henss, M. Rohnke, *Journal of Vacuum Science & Technology A* **2023**, 41.

[21] F. Walther, R. Koerver, T. Fuchs, S. Ohno, J. Sann, M. Rohnke, W. G. Zeier, J. r. Janek, *Chem. Mater.* **2019**, *31*, 3745.

[22] D. H. Tan, Y.-T. Chen, H. Yang, W. Bao, B. Sreenarayanan, J.-M. Doux, W. Li, B. Lu, S.-Y. Ham, B. Sayahpour, *Science* **2021**, *373*, 1494.

[23] X. Zhang, S. Weng, G. Yang, Y. Li, H. Li, D. Su, L. Gu, Z. Wang, X. Wang, L. Chen, *Cell Rep. Phys. Sci.* **2021**, *2*, 100668.

[24] a) B. Hertzberg, J. Benson, G. Yushin, *Electrochem. Commun.* **2011**, *13*, 818; b) L. A. Berla, S. W. Lee, Y. Cui, W. D. Nix, *J. Power Sources* **2015**, *273*, 41.

[25] J. A. Lewis, F. J. Q. Cortes, Y. Liu, J. C. Miers, A. Verma, B. S. Vishnugopi, J. Tippens, D. Prakash, T. S. Marchese, S. Y. Han, C. Lee, P. P. Shetty, H. W. Lee, P. Shevchenko, F. De Carlo, C. Saldana, P. P. Mukherjee, M. T. McDowell, *Nat. Mater.* **2021**, *20*, 503.